Ceramics International xxx (xxxx) xxx

Contents lists available at ScienceDirect

Ceramics International

journal homepage: www.elsevier.com/locate/ceramint

Synthesis, crystallographic characterization, and mechanical behavior of alumina chromia alloys

Alfredo Rondinella [a,*], Erika Furlani [a], Michele Magnan [a], Fabio Scagnetto [c], Stefano Driussi [c], Elia Marin [b], Stefano Maschio [a]

[a] University of Udine, Dipartimento Politecnico di Ingegneria Ed Architettura, Via Del Cotonificio, 108-33100, Udine, Italy
[b] Kyoto Institute of Technology, Department of Materials Sakyo-Ku, Matsugasaki, 606-8585, Kyoto, Japan
[c] FREUD Spa, Via Remigio Solari, 7, 33050, Pavia di Udine, UD, Italy

ARTICLE INFO

Keywords:
Alumina
Chromia
Crystal structure
Hardness
Raman spectroscopy

ABSTRACT

Powder mixtures of Alumina and Chromia, blended in different proportions (1, 3, 5 and 10%wt) by attrition milling, were fired either by pressureless sintering in air and hot pressing under vacuum. The resulting materials, characterized by X-ray diffraction, Raman spectroscopy, SEM, hardness and fracture toughness showed that all the compositions form complete solid solution which maintain the same crystal structures of corundum; chromia addition retards materials' densification of pressureless fired samples but not that of hot-pressed samples. Data from Raman spectroscopy and SEM/EDXS showed the appearance of Ti- and Mn-based impurities near the indentation print, in particular on fractured grains. The addition of chromia improves hardness, but does not affect toughness which is, on the other hand, greatly influenced by materials' residual porosity.

1. Introduction

Alumina is one of the oldest ceramics for technological use due to a number of properties which make it suitable for applications in different areas, such as industry, medicine, electronics and others [1]. Alumina has, for instance, high strength and hardness, but poor fracture toughness. Several researchers proposed alumina matrix composites with better toughness and strength than pure alumina materials. Such alumina-based composites include the addition of zirconia particles [2–5], SiC whiskers [6–8], metallic [9–11] or ceramic particles [12]. In addition, it is generally accepted that the formation of a vitreous phase, during the sintering of alumina powders, enables the reduction of material residual porosity, thus improving some properties of pure alumina [13]. Following another approach, it is possible to accept a low level of fracture toughness while increasing other properties. In this second approach, it is required that, when materials are "in use", they must be subjected to only compressive loads in order to limit the effects of the low fracture toughness. For example, materials made of Alumina-Chromia solid solutions are widely used to produce refractory bricks [14] or in the production of non-ferrous metal-smelter lining [15], for coal-water slurry gasifier [16] and in many other applications where their high temperature corrosion resistance is required [17–20].

Alumina-Chromia powders mixtures, when heated at high temperature, form substitutional solid solutions over the entire compositional range developing a crystal structure similar to that of pure corundum [21–23]. However, the properties of materials made of Alumina-Chromia do not depend only on their crystalline structure, but also on their microstructure [24].

It is known that the addition of chromium oxide beneficially affects the mechanical behavior of pure alumina materials. Several authors reported that the addition of chromium oxide influence the microstructural evolution and the mechanical properties of Alumina so that, when small amounts of chromium oxide are added, hardness and elastic modulus are increased [25–28]. Still remains matter of doubt the maximum content of chromium oxide which enables an improvement of alumina properties.

The present investigation refers to the processing parameters, crystal structure, density, Vickers hardness, fracture toughness and Raman spectroscopy of the alumina-chromia blends containing 1, 3, 5 and 10% wt Chromia.

2. Experimental procedure

High purity alumina powders (Sumitomo AKP15) and chromium

* Corresponding author.
E-mail address: alfredo.rondinella@uniud.it (A. Rondinella).

https://doi.org/10.1016/j.ceramint.2021.05.165
Received 14 April 2021; Received in revised form 17 May 2021; Accepted 18 May 2021
Available online 23 May 2021

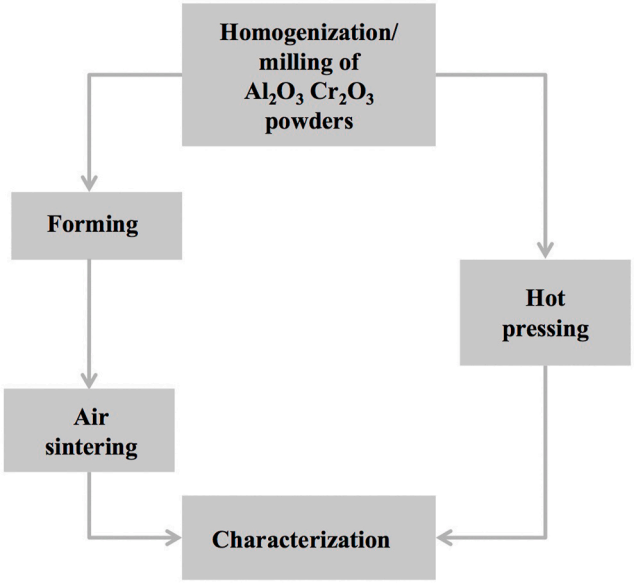

Fig. 1. Flow-chart explaining the production method of the monoliths.

oxide (Aldrich Chem 99.9%) with compositions containing 1, 3, 5 and 10% wt of Chromia (Aldrich Chem 98%) were prepared in the present investigation. Samples were named respectively C0, C1, C3, C5 and C10 to indicate their Chromia content. Powders were ball-milled for 2 h by an attritor-mill at 300 rpm in isopropanol, using alumina spheres and a highly dense cylindrical nylon container. Milling parameters were set as follows: sphere's diameter = 8 mm, jar volume = 311 cm^3, amount of isopropanol = 70 cc, amounts of balls = 480 g, amount of powder = 30 g. After milling, powders were dried in the oven at 80 °C and then stored under vacuum. After being sieved through a 63 μm sieve, powders were first uniaxially pressed at 50 MPa into cylindrical specimens (D = 15 mm, h = 3 mm) then isostatically at 200 MPa. After a preliminary sintering investigation which was made changing final temperatures and aging times to optimize the relative densities of the resulting samples, green compacts were fired for 2 h at 1550 °C. In parallel, pure alumina and mixtures of powders with compositions containing 5 and 10% wt of chromia were hot pressed (in nitrogen) by a home-made apparatus, at 1500 °C and 50 MPa for 10 min into cylindric disks (D = 32 mm and h = 5 mm). For comparison, a set of pure alumina samples was also prepared using the same processing parameters as for the Alumina-Chromia blends. A simple flow chart explaining the production methods used for the monoliths is shown in Fig. 1.

In order to test powders particles size distribution (PSD) after the milling process, a Horiba LA950 laser scattering particle size distribution analyzer was used; analyses were made in water after sonication for 3 min.

The apparent densities of the fired samples were manually measured following the Archimedes' water displacement method explained in the EN 623–2:1993.

XRD patterns were recorded on a Philips X'Pert diffractometer setting the operation conditions at 40 kV and 40 mA using nickel-filtered Cu-Kα radiation. Spectra were collected using a step size of 0.02° and a counting time of 40s per angular abscissa in the range 20°–80°. Rietveld refinement were used to calculate the theoretical densities of the solid solutions [29].

Hardness was determined by a Vickers indenter applying a load of 100 N; the same automated equipment was used to evaluate fracture toughness which was accessed following the indentation fracture (IF) method (Evans and Charles equation [30]) on polished (1 μm) diamond paste surfaces. Toughness and hardness values were averages of ten readings.

Samples were also investigated by mean of Raman spectroscopy. Spectra were collected using a Raman Spectrometer (RAMANtouch instrument, Laser RAMAN Microscope of Nanophoton Corp, Osaka, Japan) supplied with a 532 nm green excitation line and a charge coupled device (CCD) camera (400 × 1340-pixel). The spectrometer operated with confocal imaging mode and acquired Raman spectral maps in two dimensions. A commercially available software (Raman Viewer, Laser RAMAN Microscope of Nanophoton Corp, Osaka, Japan), was used to analyze the collected spectral data and to build intensity maps.

Microstructures were examined by a scanning electron microscope (SEM) coupled with an X-ray spectrometer microprobe analyzer (EDAX) on polished (1 μm diamond paste) and thermally etched surfaces (1450 °C, ½ h). Average grain size was accessed by the lineal intercept method on 5000x SEM images.

3. Results and discussion

Fig. 2 shows the PSD of the powders with composition C10 after the milling procedure; however all the compositions display the same

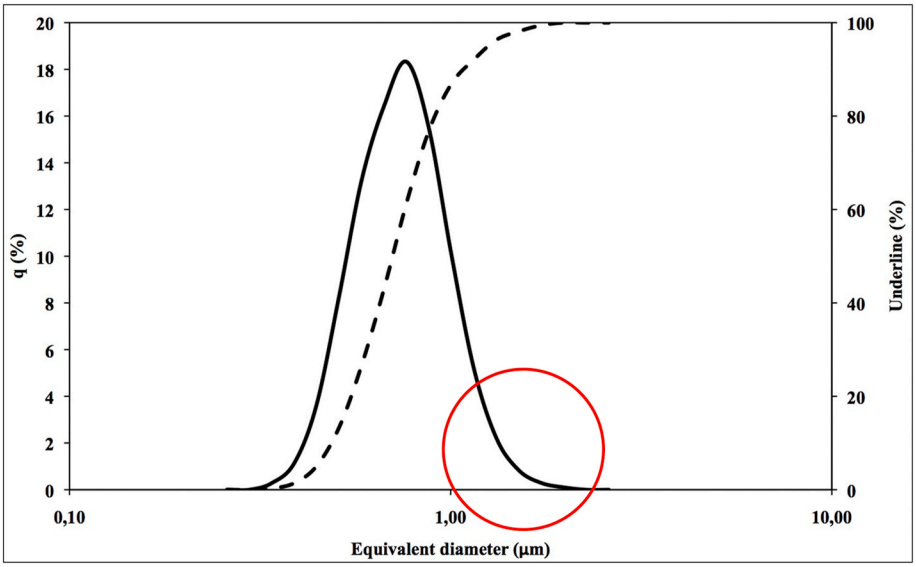

Fig. 2. Particle size distribution (PSD) of the powders with composition C10 after the milling procedure.

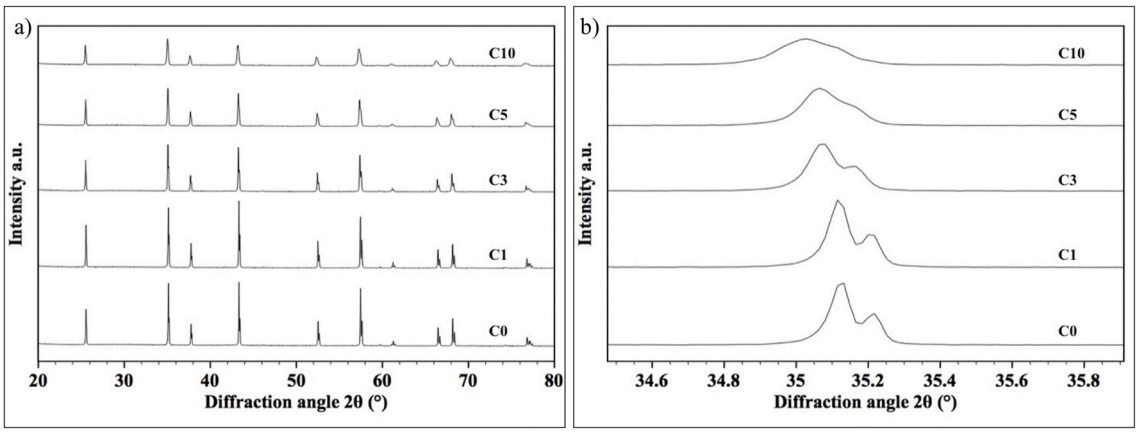

Fig. 3. X-ray diffraction patterns, between 20 and 80° of the samples C0–C10 fired in air (a) and detail between 34.5 and 35.9° of the XRD patterns of samples C0–C10 fired in air (b).

Table 1
Composition, symbolic name, apparent, theoretical, relative density and average grain size of the materials prepared.

Composition	Symbolic name	Apparent density (g/cm^3)	Theoretical density (g/cm^3)	Relative density (%)	Average grain size (μm)
Al_2O_3	C0	3.93	3.97	99.0	2.8
1% wt Cr_2O_3	C1	3.94	3.97	99.3	2.6
3% wt Cr_2O_3	C3	3.95	3.99	99.1	1.45
5% wt Cr_2O_3	C5	3.89	4.01	97.0	1.35
10% wt Cr_2O_3	C10	3.78	4.06	93.1	0.95
Al_2O_3-HP	C0HP	3.94	3.97	99.3	1.05
5% wt Cr_2O_3-HP2	C5HP	3.98	4.01	99.4	1.0
10% wt Cr_2O_3-HP	C10HP	4.03	4.06	99.2	1.0

distribution. It can be observed a monomodal PSD, with a peak of particles with dimension of 0.8 μm, but also containing particles having dimensions ranging from 1 to 3 μm which may play a role on the microstructure of fired materials. In particular, the particles which belong to the circled range in Fig. 2 reasonably affect homogeneity of materials chemical composition after the sintering process.

Fig. 3a shows the X-ray diffraction peaks of the samples C0–C10. All the compositions form complete solid solution which maintain the same crystal structures of corundum; no other solutions or compounds have been revealed.

However, the lattice parameters, calculated through Rietveld refinement [29], varied with the Chromia content changing the theoretical density of the different compositions. They are displayed in Table 1 which also reports apparent and relative density of the fired samples.

It can be also observed, according to the results obtained by other authors [31,32], that the addition of Chromia to Alumina causes enlargement and shifting of the peak 104 towards lower angle in comparison with pure alumina samples and, at the same time, its intensity is reduced. This statement is documented in Fig. 3b and reveals a

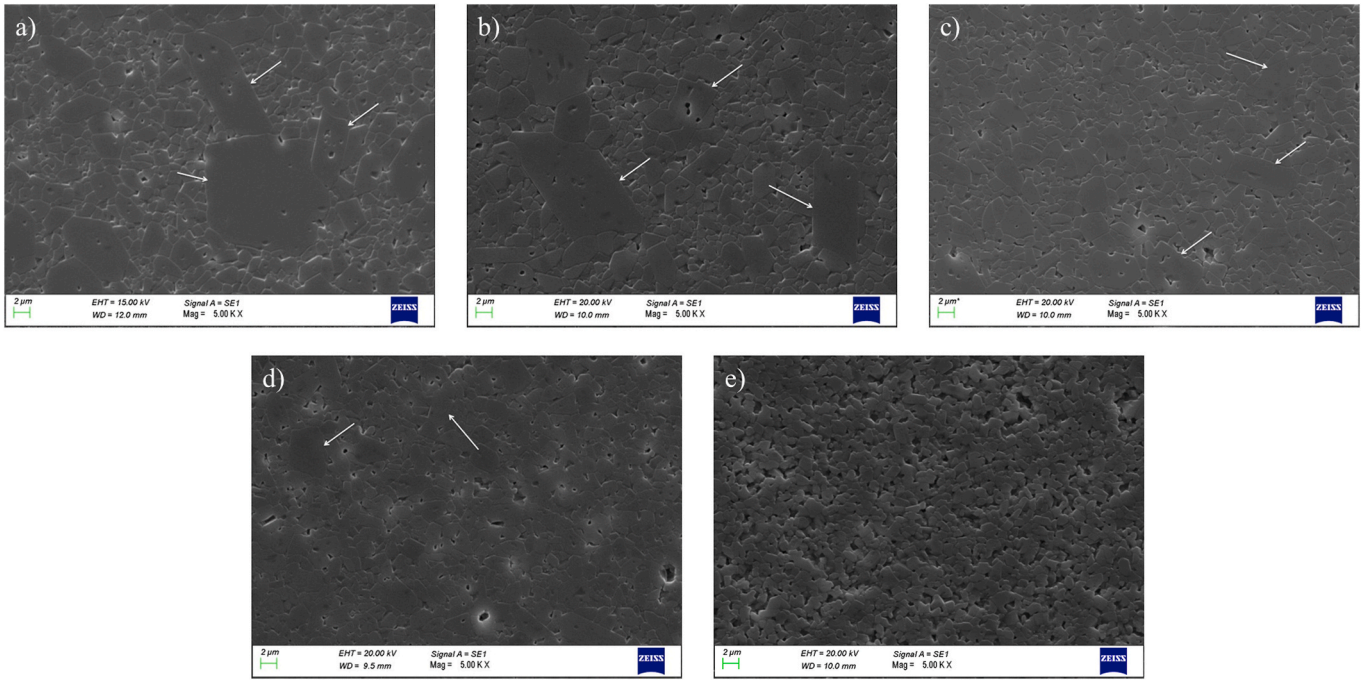

Fig. 4. SEM microstructures (5000x) of C0 (a), C1 (b), C3 (c), C5 (d) and C10 (e) samples fired in air.

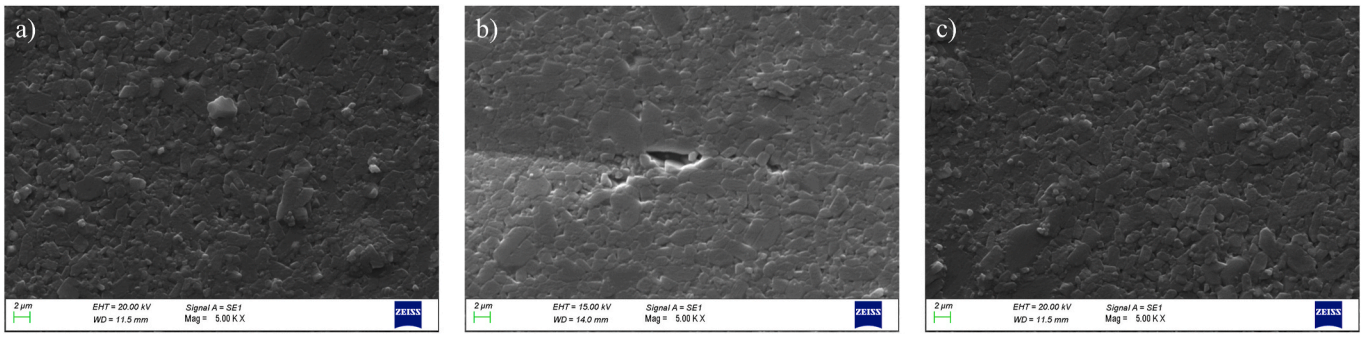

Fig. 5. SEM microstructures (5000x) of hot-pressed samples C0HP (a), C5HP (b) and C10HP (c).

progressive increase of the crystallite size inside the grains of the solid solutions [29]. The XRD patterns acquired on hot pressed samples did not show differences with those of materials pressureless fired in air.

Table 1 shows that, materials sintered in air display the maximum values of relative density in compositions containing 1 and 3% wt Chromia, whereas greater amounts chromium oxide lead to lower values. Conversely, hot pressing permits to reach relative density values greater than 99% in all compositions.

Table 1 also shows the average grain size of the materials: it can be observed that values range from 2.8 μm measured in the reference sample, to 0.95 in C10. Materials hot pressed display almost the same average grain size which is around 1 μm. Fig. 4 show the microstructures of samples C0, C1, C3, C5 and C10 from **panel (a)** to **panel (e)**, respectively. It can be observed that samples with composition C0, C1 C3 and C5, contain a great number of grains with dimension close to their average size, together with several abnormally grown grains (indicated by white arrows in Fig. 4). The broadening of the XRD peaks as well as the presence of abnormally grown grains could be due to a non-uniform distribution of Chromia in solution as highlighted by the powders particles size distribution after milling.

Their size ranges from 10 to 15 μm in C0, 9 and 12 μm in C1, from 5 to 8 in C3 and 4 and 7 μm in C5 whereas C10 shows a much more uniform microstructure whose grains have dimensions around the average size. On the other hand, all hot-pressed samples display homogeneous microstructures, as shown in Fig. 5. It seems reasonably to state that the addition of chromium oxide lowers alumina's grain boundaries diffusion at high temperature in this way retarding densification and consequently grains coalescence. Residual porosity increases, in accordance with the results obtained by other authors [26,27,32]. Hot pressed materials display microstructures which seem to be not affected by the amount of added chromia.

Coble [33,34] suggested, in absence of the liquid phase, four steps for the sintering process:

1. Powders particles, loosely packed with low initial relative densities, form an interconnected network of pores. As the body sinters there is no change in the mean grain size;
2. Takes over from the early stage at relative density around 0.6%. The pore structure remains similar as that of stage 1, but densification is now associated to grain growth;
3. Occurs when the pores coalesce and grains continue to grow. This stage take place at relative density of about 0.95;
4. The migrating grain boundaries break away from the pores entrapping them into the grains, densification essentially stops, whereas grains continue to grow at high rate.

Table 1 and Fig. 3 show that composition C0, C1 and C3 have reached the fourth stage of sintering proposed by Coble under the sintering conditions followed in the present research, whereas compositions C5 and C10 seems to reach the third sintering stage. In addition, it could be assumed that C0, C1 and C3 suffer from an overfiring thermal treatment, whereas samples with composition C5 and C10 appear not completely densified.

Fig. 6a displays Vickers hardness (plain line) and fracture toughness (dashed line) vs Chromia content of the samples fired in air. It is observed that hardness starts from 14.4 GPa of pure alumina, reaches the maximum of 15 GPa in C3 and decreases to 9.7 in C10. Toughness maintains a constant value of 4.3 MPa $m^{1/2}$ on compositions C0–C3 and lowers to 4.2 and 3.9 MPa $m^{1/2}$ on compositions C5 and C10 respectively. The above values should take account the relative density of the corresponding materials. Table 1 shows that compositions C0, C1 and C3 have relative density equal or higher that 99% of theoretical density, but lower to 97.0 and 93.1% in compositions C5 and C10 respectively. It appears reasonable that hardness and toughness reduction of composition C5 and C10 could be attributed to their relatively high porosity.

Fig. 6b shows Vickers hardness (plain line) and fracture toughness (dashed line) vs Chromia content of hot-pressed samples. It can be

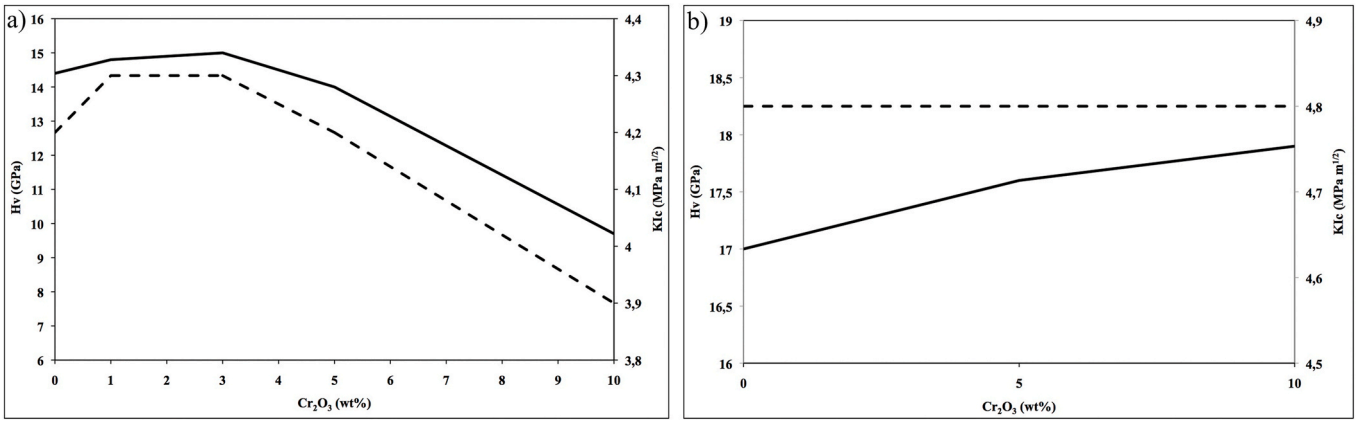

Fig. 6. Vickers hardness (plain line) and fracture toughness (dashed line) vs Chromia content of fired in air (a) and hot-pressed (b) samples.

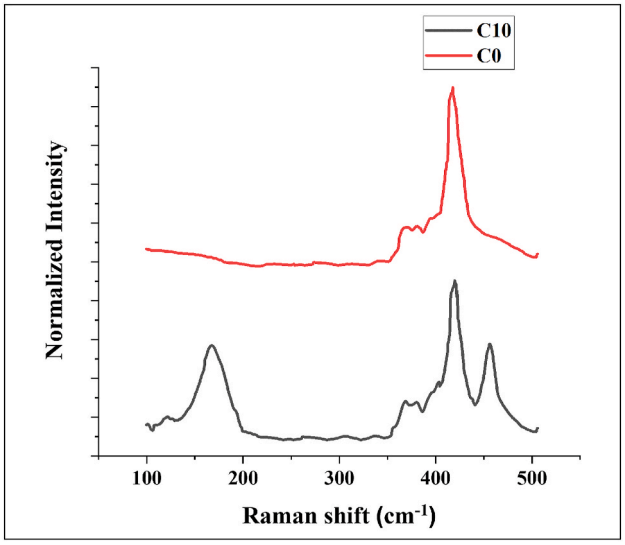

Fig. 7. Raman spectra of a C0 and a C10 sample.

observed that toughness remains constant at 4.8 MPa $m^{1/2}$ whereas hardness increases from 17 GPa of pure alumina to 17.6 of composition C5HP and 17.9 of C10HP. The relative density is greater than 99% theoretical density in all the samples. It may be concluded that relative density has same influence on all those compositions being negligible the influence of the residual porosity. On the other hand, the addition of chromia improves hardness, but does not affect toughness in accordance with literature data [25].

Raman spectral maps were collected on the area surrounding the Vickers print on all the samples and showed the appearance of two unexpected peaks. Their occurrence and intensity increased with the amount of Chromia in the samples.

Fig. 7 compares the normalized Raman spectra of a C0 and a C10 sample. Three major peaks appear in the area of interest: at 146, 415 and 460 cm^{-1}. The Raman band at 415 cm^{-1} can be attributed to the Alumina [35,36]. It could be hypothesized that the vibrations at 146 and 460 cm^{-1} are due to the presence of TiO_2, a common impurity found in Chromia which has a strong Raman signal [37,38]. It was not possible to observe the signal from Chromia, probably because its weak Raman signal is obscured by more intense peaks.

The presence of these three peaks was mapped along the crack generated by the indentation, revealing that the two TiO_2 peaks appeared mostly on damaged points. Fig. 8 displays some of the collected maps, for a C0, a C5 and a C10 sample, respectively. The area marked by the white rectangle tracks the indentation. It was not possible to focus the laser spot in these areas, for this reason the spectra from the indentation prints are not to take into account for the detection of the two TiO_2 Raman bands.

Fig. 8b) and c) show how the bands at 146 and 460 cm^{-1} appear

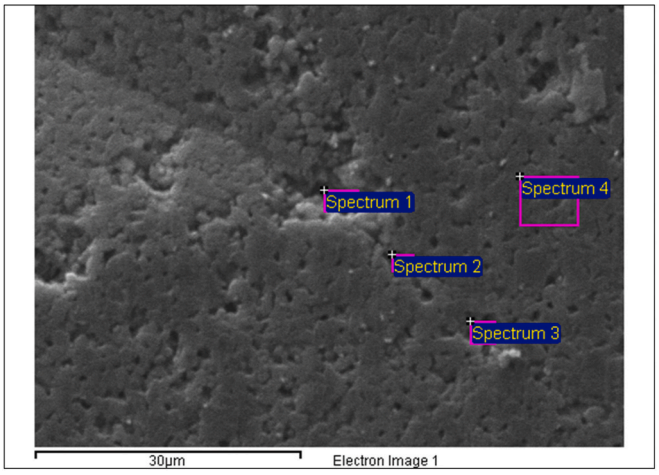

Fig. 9. Indentation crack for a C10 sample showing the areas investigated by EDXS.

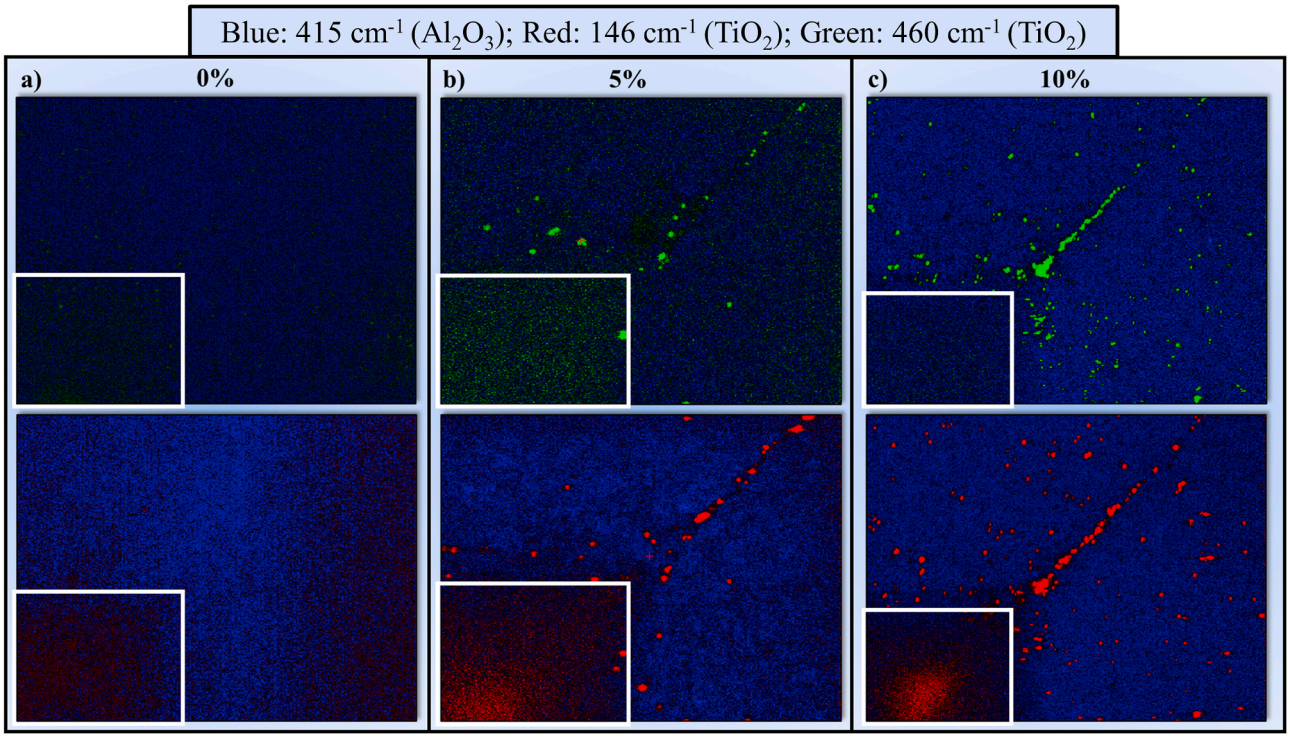

Fig. 8. Raman spectral maps for a C0 (a), a C5 (b) and a C10 (c) sample.

Table 2
Chemical analysis for the areas shown in Fig. 9.

Spectrum	O	Mg	Al	Ti	Cr	Mn	Zn	Total
Spectrum 1	38.40		45.76	0.11	15.65		0.08	100.00
Spectrum 2	39.35	0.13	49.90	0.04	10.55	0.04		100.00
Spectrum 3	38.41	0.04	49.75	0.06	11.68	0.05		100.00
Spectrum 4	44.83		46.96		8.22			100.00

mostly along the indentation crack and in surrounding areas, where grains are fractured. Normally, such impurities, would be found at the grain boundaries [39,40] but in this case they are found inside fractured areas.

SEM and EDXS analyses were performed in the same areas investigated by Raman spectroscopy, to find confirmation about the findings from the Raman maps. Fig. 9 shows the surface morphology of the indentation on a C10 sample. The crack generated by the print and the area investigated by EDX spectroscopy are clearly visible. Table 2 illustrates the results of the chemical analysis and shows that Ti is present inside the crack, while its signal is absent outside. This validates the hypothesis made about the results from the Raman spectroscopy investigation.

These findings could be explained by mean of two possible, not necessarily alternative mechanisms. In the first one, it is hypothesized that the grain is composed of two regions: a core and a shell, as explained by Riu et al. [25]. The core is external part of the grain, exposed to the environment and is composed of only alumina, while the core contains the impurities. Once the crack appears, the grain gets fractured, and the impurities emerge and the strong TiO_2 signal is visible along the crack.

The second possible mechanism could have the following explanation. The TiO_2–MnO_2 binary phase diagram shows that the liquid phase appears at 1320 °C in composition 1:1 at as shown by Huang et al., [42]. The presence of those compounds as impurities of the Chromia starting powder, causes therefore a certain quantity of liquid phase during the sintering process; it is also assumed that the liquid phase is formed on heating during sintering (as mentioned in experimental procedure). Impurities therefore accumulates along grain boundaries and inside triple points [41,42], but are exposed as a consequence of the grain fracture and of the increase of the material free surface [43,44].

As conclusive consideration, the present research demonstrates that the addition of chromia to alumina leads to the production of materials with higher hardness with respect to alumina alone; conversely, toughness seems to be not affected by the presence of chromia. In fact, toughness changes between materials with different composition have been measured, but they reasonably occurred as a consequence of their microstructure, i.e., residual porosity and grain size distribution. Chromium oxide retards alumina high temperature diffusion processes which lead to material's densification. It follows that the addition of chromia imply the use of much more expensive thermal treatments, such as higher temperatures, longer aging time or use of hot pressing. Materials with chromia content equal or inferior to 3% wt, produced by "in air pressureless sintering" could be a good compromise.

4. Conclusion

Alumina and Chromia (1, 3, 5, 10 wt%) mixtures were produced by attrition milling. Each batch was fired by pressureless sintering in air and hot pressing under vacuum. The resulting materials were characterized by X-ray diffraction, Raman spectroscopy, SEM, hardness and fracture toughness.

XRD analysis showed that all the compositions form complete solid solution which maintain the same crystal structures of corundum and no other solutions or compounds have been revealed. SEM analysis demonstrated that C0, C1 and C3 suffer from an overfiring thermal treatment, whereas samples with composition C5 and C10 appear not completely densified.

Vickers hardness tests display values from 14.4 GPa of pure alumina, reach the maximum of 15 GPa in C3 and decrease to 9.7 in C10. Toughness maintains a constant value of 4.3 MPa $m^{1/2}$ on compositions C0–C3 and lowers to 4.2 and 3.9 MPa $m^{1/2}$ on compositions C5 and C10 respectively.

The analysis of the areas surrounding indentation, showed that presence of TiO_2 impurities in, in particular on the indentation crack. This could be explained by either the formation of a core-shell morphology inside the grain or the presence of a liquid phase accumulated inside the grain boundaries and the triple points. Findings from Raman spectroscopy and SEM/EDXS showed that the impurities are exposed after indentation and the subsequent grain fracture.

Declaration of competing interest

The authors declare that they have no known competing financial interests or personal relationships that could have appeared to influence the work reported in this paper.

Acknowledgement

The authors would like to express their gratitude to Sumitomo Italy for kindly supplying the AKP 15 alumina powder.

References

[1] E. Dorre, H. Hubner, Alumina, Springer-Verlag, Berlin, Heidelberg, New York, Tokyo, 1984.
[2] N. Claussen, J. Steeb, R.F. Pabst, Effect of induced microcracking on the fracture toughness of ceramics, Am. Ceram. Soc. Bull. 56 (6) (1977) 559–562.
[3] T. Kosmac, M.V. Swain, N. Claussen, The role of tetragonal and monoclinic ZrO_2 particles in the fracture toughness of alumina-ZrO_2 composites, Mater. Sci. Eng. 71 (1985) 57–64.
[4] S. Hori, M. Yoshimura, S. Somiya, R. Kurita, H. Kaji, Mechanical properties of ZrO_2-toughened alumina ceramics from CVD powders, J. Mater. Sci. Lett. 4 (1985) 413–416.
[5] M. Ruhle, N. Claussen, A.H. Heuer, Transformation and microcrack toughening as complementary processes in ZrO_2-toughened alumina, J. Am. Ceram. Soc. 69 (3) (1986) 195–197.
[6] G.H. Campbell, M. Ruhle, B.J. Dalgleish, A.G. Evans, Whisker toughening: a comparison between aluminum oxide and silicon nitride toughened with silicon carbide, J. Am. Ceram. Soc. 73 (3) (1990) 521–530.
[7] P.F. Becker, G.C. Wei, Toughening behavior in SiC-Whisker-Reinforced alumina, J. Am. Ceram. Soc. Com. 67 (12) (1984) C267–C269.
[8] T.E. Steyer, K.T. Faber, Mechanical behavior of alumina reinforced with carbon-coated silicon carbide whiskers, J. Am. Ceram. Soc. 78 (10) (1995) 2673–2679.
[9] C.O. McHugh, T.J. Whalen, M. Humenik Jr., Dispersion-strengthened aluminum oxide, J. Am. Ceram. Soc. 49 (9) (1966) 486–491.
[10] L.S. Sigl, P.A. Mataga, B.J. Dalgleish, R.M. McMeeking, A.G. Evans, On the toughness of brittle materials reinforced with a ductile phase, Acta Metall. 36 (4) (1988) 945–953.
[11] B.D. Flinn, C.S. Lo, F.W. Zok, A.G. Evans, Fracture characteristics of a metal-toughened ceramic, J. Am. Ceram. Soc. 76 (2) (1993) 369–375.
[12] R.P. Wahi, B. Ilschner, Fracture behavior of composites based on alumina-TiC, J. Mater. Sci. 15 (1980) 875–885.
[13] J.D. Birchall, J.A.A. Bradbury, J. Dinwoodie, Handbook of composites, in: W. Watt, B.V. Perov (Eds.), Cap. IV: Strong Fibres, vol. I, Elsevier, Amsterdam, 1985.
[14] Y. Murakami, T. Hirata, Y. Tsuru, Metastable phase relationship in the Al2O3-Cr2O3 system and phase equilibria of 1:1 composition at 1200°C, J. Ceram. Soc. Jpn. 110 (2002) 541–543.
[15] P. Gehre, C.G. Aneziris, H. Berek, et al., Corrosion of magnesium aluminate spinel-rich refractories by Sulphur-containing slag, Eur. Ceram. Soc. 35 (2015) 1613–1620.
[16] L.I. Youqi, K.E. Changming, G.A.O. Song, et al., Effects of zirconia on the thermal shock resistance of high chrome refractories for coal slurry gasifier, in: Proceedings UNITECR'13, British columbia, Canada, 2013, pp. 1127–1132.

[17] J.P. Kiehl, Y. Le Mat, Use of chrome–alumina castables and shapes in blast furnace and carbon black reactors, Ceram. Bull. 62 (7) (1983) 809–810.
[18] T. Hirata, T. Morimoto, S. Ohta, N. Uchida, Improvement of the corrosion resistance of alumina–chromia ceramic materials in molten slag, J. Eur. Ceram. Soc. 23 (2003) 2089–2096.
[19] T.J. Davies, H.G. Emblem, A. Harabi, C.S. Nwobodo, A.A. Ogwu, V. Tsantzalou, Characterisation and properties of alumina–chrome refractories, J. Br. Ceram. Trans. 91 (1992) 71–76.
[20] D. Chen, A. Huang, H. Gu, M. Zhang, Z. Shao, Corrosion of Al2O3–Cr2O3 refractory lining for high-temperature solid waste incinerator, Ceram. Int. 41 (2015) 14748–14753, https://doi.org/10.1016/j.ceramint.2015.07.202.
[21] I. Levin, D. Brandon, Metastable alumina polymorphs: crystal structures and transition sequences, J. Am. Ceram. Soc. 2012 (2012), 1995–2012.
[22] J. Graham, Lattice spacings and colour in the system alumina-chromic oxide, J. Phys. Chem. Solid. 17 (1960) 18–25, https://doi.org/10.1016/0022-3697(60)90170-0.
[23] E.N. Bunting, Phase equilibria in the system Cr2O3-Al2O3, J. Res. Natl. Bur. Stand. 6 (1931) 947–949. http://refhub.elsevier.com/S1044-5803(15)30045-0/rf0005.
[24] F. Bondioli, A.M. Ferrari, C. Leonelli, T. Manfredini, L. Linati, P. Mustarelli, Reaction mechanism in alumina/chromia (Al2O3–Cr2O3) solid solutions obtained by coprecipitation, J. Am. Ceram. Soc. 83 (2000) 2036–2040. http://refhub.elsevier.com/S1044-5803(15)30045-0/rf0010.
[25] D.-H. Riu, Y.-M. Kong, H.-E. Kim, Effect of Chromia addition on microstructural evolution and mechanical properties of Alumina", J. Eur. Ceram. Soc. 20 (2000) 1475–1481.
[26] A. Harabi, T.J. Davies, Mechanical-properties of sintered alumina chromia refractories, Br. Ceram. Trans. 94 (1995) 79–84.
[27] M. Fujita, K. Inukai, S. Sakida, T. Nanba, J. Ommyoji, A. Yamaguchi, Y. Miura, Sintering of Alumina–Chromia powder prepared by sol–gel process, J. Soc. Mater. Sci. Jpn. 56 (2007) 526–530.
[28] A. Harabi, T.J. Davies, Densification and grain-growth in sintered alumina–chromia powder mixtures, Br. Ceram. Trans. 94 (1995) 97–102.
[29] R. Jenkins, R. Snyder, Introduction to X-Ray Powder Diffractometry, Wiley, New York, 1996.
[30] B.R. Lawn, A.G. Evans, A model for crack initiation in elastic/plastic indentation fields, J. Mater. Sci. 12 (11) (1977) 2195–2199.
[31] P. Zhao, H. Zhao, J. Yu, H. Zhang, H. Gao, Q. Chen, Crystal structure and properties of Alumina-Chromia solid solutions with different Chromia contents, Ceram. Int. 44 (2018) 1356–1361, https://doi.org/10.1016/j.ceramint.2017.08.195.
[32] M. Nath, S. Sen, K. Banerjee, A. Ghosh, H.S. Tripathi, Densification behavior and properties of alumina-chrome ceramics: effect of TiO_2, Ceram. Int. 39 (2013) 227–232, https://doi.org/10.1016/j.ceramint.2012.06.013.
[33] R.L. Coble, Sintering Crystalline solids. I. Intermediate and final state diffusion models, J. Appl. Phys. 32 (1961) 787–792, https://doi.org/10.1063/1.1736107.
[34] R.L. Coble, Sintering Crystalline solids. II. Experimental test of diffusion models in powder compacts, J. Appl. Phys. 32 (1961) 793–798, https://doi.org/10.1063/1.1736108.
[35] S. Tochino, W.L. Zhu, T. Sawada, J. Ikeda, G. Pezzotti, Spatially resolved Raman spectroscopy for In-depth non-destructive residual stress and phase transformation assessments in 3Y-TZP bioceramics, Key Eng. Mater. 309 (2006) 1203–1206 (Trans Tech Publications Ltd).
[36] W. Zhu, G. Pezzotti, Tensor and spatially resolved analysis of microscopic stress fields in polycrystalline alumina by polarized Raman spectroscopy, Phys. Status Solidi 208 (5) (2011) 1141–1150.
[37] M.N. Iliev, V.G. Hadjiev, A.P. Litvinchuk, Raman and infrared spectra of brookite (TiO2): experiment and theory, Vib. Spectrosc. 64 (2013) 148–152.
[38] O. Frank, M. Zukalova, B. Laskova, J. Kürti, J. Koltai, L. Kavan, Raman spectra of titanium dioxide (anatase, rutile) with identified oxygen isotopes (16, 17, 18), Phys. Chem. Chem. Phys. 14 (42) (2012) 14567–14572.
[39] Y. Ikuhara, H. Yoshida, T. Sakuma, Impurity effects on grain boundary strength in structural ceramics, Mater. Sci. Eng., A 319 (2001) 24–30.
[40] Y. Ikuhara, P. Thavorniti, T. Sakuma, Solute segregation at grain boundaries in superplastic SiO_2-doped TZP, Acta Mater. 45 (12) (1997) 5275–5284.
[41] X.W. Huang, S.W. Wang, S.K. Zhao, X.X. Huang, Effect of liquid-forming additives on the sintering and mechanical properties of Alumina/3Y-TZP (30 vol.%) composite, Mater. Res. Bull. 37 (10) (2002) 1709–1719.
[42] X.W. Huang, J.C. Yu, Q. Li, X.D. Huang, X.Q. Li, X.L. Liu, Microstructure and mechanical properties of 3Y-TZP/Alumina composites fabricated by liquid phase sintering, J. Mater. Sci. 40 (7) (2005) 1693–1697.
[43] X.W. Huang, S.W. Wang, X.X. Huang, Influence of sintering aids on sintering and mechanical properties of 3Y-TZP/Al_2O_3 (40 vol%) composite, J. Mater. Sci. Lett. 21 (18) (2002) 1439–1443.
[44] S. Ramesh, S. Meenaloshini, C.Y. Tan, W.K. Chew, W.D. Teng, Effect of manganese oxide on the sintered properties and low temperature degradation of Y-TZP ceramics, Ceram. Int. 34 (7) (2008) 1603–1608.